JGR Solid Earth

RESEARCH ARTICLE
10.1029/2019JB018023

Key Points:
- Lithic component data can be used to study conduit geometry evolution during explosive eruptions and constrain eruptive parameters
- The onset of the Plinian phase of the 79 CE Vesuvius eruption was characterized by intense crater excavation processes
- Exit pressure and velocity decreased during all the Plinian phase of this event, consistent with a shift to a collapsing column dynamics

Supporting Information:
- Supporting Information S1

Correspondence to:
A. Aravena,
alvaro.aravenaponce@unifi.it

Citation:
Aravena, A., Cioni, R., de' Michieli Vitturi, M., & Neri, A. (2019). The lithic component of pyroclastic deposits as a proxy for the reconstruction of the syneruptive evolution of volcanic conduits: The CE 79 eruption of Vesuvius. *Journal of Geophysical Research: Solid Earth*, *124*, 11,022–11,037. https://doi.org/10.1029/2019JB018023

Received 15 MAY 2019
Accepted 1 OCT 2019
Accepted article online 22 OCT 2019
Published online 16 NOV 2019

The Lithic Component of Pyroclastic Deposits as a Proxy for the Reconstruction of the Syneruptive Evolution of Volcanic Conduits: The CE 79 Eruption of Vesuvius

A. Aravena[1], R. Cioni[1], M. de' Michieli Vitturi[2], and A. Neri[2]

[1]Dipartimento di Scienze della Terra, Università di Firenze, Firenze, Italy, [2]Istituto Nazionale di Geofisica e Vulcanologia, Sezione di Pisa, Pisa, Italy

Abstract Dynamics of explosive eruptions is often strongly controlled by temporal changes in conduit geometry. Quantitative constraints to this problem are difficult to define, but basic information on the lithic fraction in pyroclastic deposits can be used as an input of numerical models to infer conduit and crater evolution in terms of shape and dimension. Field data on the 79 CE Pompeii eruption (Vesuvius, Italy) are used here to constrain depth-dependent variations in conduit geometry. The different lithology of the accidental components, resulting from the erosion of a conduit/crater system crosscutting a well-known subsurface stratigraphy, helps in defining the provenance depth of the eroded fragments. We reproduced the eruption evolution by considering three periods of the Plinian phase, associated with the white phonolitic pumice clasts (EU2a) and the tephro-phonolitic gray pumice clasts (EU3a and EU3b). Results constrain the evolution of key eruptive parameters and are consistent with the estimates of mass discharge rate (MDR) and volume of eroded lithic fragments, which require the involvement of conduit geometries with depth-dependent diameters rather than a constant-radius shape. The onset of the Plinian phase (EU2a) was characterized by intense crater excavation processes. The MDR increase during the transition from EU2 to EU3 coincided with a significant increase of conduit diameter at bottom. After the peak of MDR (EU3b), a significant deeping of the fragmentation level and an abrupt inlet pressure drop probably occurred. Exit pressure and velocity would have decreased during all the Plinian phase, consistent with a shift to a collapsing column dynamics.

1. Introduction

The analysis of pyroclastic deposits provides the fundamental information for understanding the behavior of explosive eruptions. From the study of the dispersal features and thickness of pyroclastic fall deposits, we are able to deduce useful data for estimating the intensity and magnitude of volcanic eruptions (Bonadonna & Costa, 2012; Carey et al., 1995; Carey & Sigurdsson, 1989; Pyle, 1989), which represent key information for volcanic hazard assessment (Connor et al., 2001; Macedonio et al., 2008; Macedonio et al., 2016). The detailed analysis of juvenile fragments can provide valuable information for understanding a wide family of volcanological processes, such as changes in magma ascent dynamics (Cashman, 1988; Cioni et al., 1992; Gurioli et al., 2005; Shea et al., 2010; Vinkler et al., 2012), interaction with external water (Aravena et al., 2018; Barberi et al., 1989; White & Valentine, 2016; Wohletz, 1986), and the nature of magma fragmentation (Büttner et al., 2006; Klug & Cashman, 1996; Spieler et al., 2004; Vinkler et al., 2012). Crystal content, size distribution and composition have been widely employed for studying pre-eruptive conditions of magma reservoirs and syn-eruptive conduit processes, where the use of geochemical tools is frequently involved (Blundy & Cashman, 2001; Cioni et al., 2014; Gurioli et al., 2005; Hammer et al., 1999; Shea et al., 2009). Still, the state of the art for interpreting pyroclastic deposits is quite limited when we study some additional features, such as the nature and volume of lithic fragments. Therefore, part of the potential information that pyroclastic deposits can provide may be systematically dismissed. Indeed, even considering that lithic fragments can represent a significant part of pyroclastic deposits, the factors controlling their inclusion in the erupted mixture are still poorly understood, as well as the effects of conduit geometry on the eruptive dynamics.

Lithic fragments in pyroclastic fall deposits can derive from erosion of the conduit walls (fluid shear stress, pyroclast impact), from collapse processes of the conduit/crater system, and/or from crater excavation near the surface (i.e., mechanical erosion of the vent produced by the high-pressure, high-velocity erupted mixture) (Aravena et al., 2017; Doubik & Hill, 1999; Eichelberger & Koch, 1979; Harp & Valentine, 2015; Keating et al., 2008; Macedonio et al., 1994; Valentine et al., 2007). Macedonio et al. (1994) presented a pioneering work on the analysis of conduit erosion mechanisms and the content of lithic fragments in pyroclastic deposits, using the 79 CE Vesuvius eruption for illustrating their observations, and two recent works addressed the mechanical stability of volcanic conduits using an approach based on numerical modeling (Aravena et al., 2017; Aravena et al., 2018). Since conduit widening is controlled by country rock mechanical properties and the pressure and velocity profiles along the conduit (Aravena et al., 2017; Macedonio et al., 1994; Varekamp, 1993), the volume and type of lithic fragments eroded from the conduit can be potentially employed for studying the internal dynamics of volcanic conduits and their geometric features whenever the subsurface stratigraphy is known. For example, the geometric evolution of the feeding system of the Pomici di Avellino eruption was recently studied by Massaro et al. (2018). The main sources of uncertainty of these methods are associated with the necessity of fixing simplified models to describe conduit geometry and the nature of the procedure adopted to quantify the lithic content. In particular, Massaro et al. (2018) assumed that a volcanic conduit evolves from a dyke connected to the surface to a hybrid dyke/cylinder feeding system. Their model does not consider crater excavation, and conduit erosion is preferentially concentrated in the deep domain of the conduit. However, considering the mechanisms of conduit erosion during explosive eruptions (Aravena et al., 2017; Macedonio et al., 1994), plausible conduit geometries are expected to be characterized by larger dimensions near the vent, associated with the occurrence of conduit collapses above the fragmentation level, pyroclast impact, and crater excavation (Doubik & Hill, 1999; Valentine & White, 2012).

In this work, we use quantitative lithic component information on the 79 CE Vesuvius eruption and conduit modeling to make estimates of syn-eruptive changes in conduit geometry, considering three main periods during the Plinian phase of the eruption. The well-known subsurface stratigraphy (Bernasconi et al., 1981; Brocchini et al., 2001) and the availability of useful works for constraining the input parameters and constitutive equations of numerical simulations support the choice of this case study (Carey & Sigurdsson, 1987; Cioni, 2000; Cioni et al., 1992; Cioni et al., 2000; Neri et al., 2003; Shea et al., 2009; Shea et al., 2012). Numerical modeling is also based on field data complemented with literature-derived information, which allowed to calculate the volume and mass of the different types of lithic fragments present in the pyroclastic deposits through the use of isomass and isopach maps. In this way, MDR-controlled changes in the dispersal area and density differences between lithic fragments and vesicular, low-density pyroclasts (and thus, differences in their terminal velocities and spatial distribution in pyroclastic deposits) do not bias the estimates of the proportion of the different components present in the pyroclastic deposits. We remark that this is not true when height-normalized sections are used to quantify the evolution of lithic content during an eruption. This work includes five parts. First, we present the geologic framework of this case study. Then, we describe the methods, including the treatment of field data and the conduit model adopted here. Third, we present the results associated with the use of field data; followed by the numerical modeling results. Finally, we Qpresent the discussions and conclusions associated with this investigation, providing constraints to the evolution of key eruptive parameters during the event and showing that conduit geometries with depth-variable dimensions are needed to reproduce the different phases of this eruption.

2. Geologic Framework

Somma-Vesuvius volcanic complex (SVVC) is a composite volcano located in Southern Italy (Figure 1a). It has been active during the last 39 ka and its products are mainly associated with the emission of silica-undersaturated potassium-rich magmas (Di Renzo et al., 2007; Santacroce et al., 2008). Because SVVC is located in the metropolitan area of Napoli (>1 million inhabitants) and because it has produced different eruptive phenomena over its history, from lava flows to large pyroclastic flows and fallout deposits, Vesuvius volcano poses important challenges for volcanic hazard and risk assessment (Neri et al., 2008). Several sub-Plinian and Plinian eruptions are recognized in the pyroclastic record of SVVC, which have been studied extensively during the last decades (Cioni et al., 1999; Cioni et al., 2008; Lirer et al., 1973; Sigurdsson et al., 1985; Sulpizio et al., 2010).

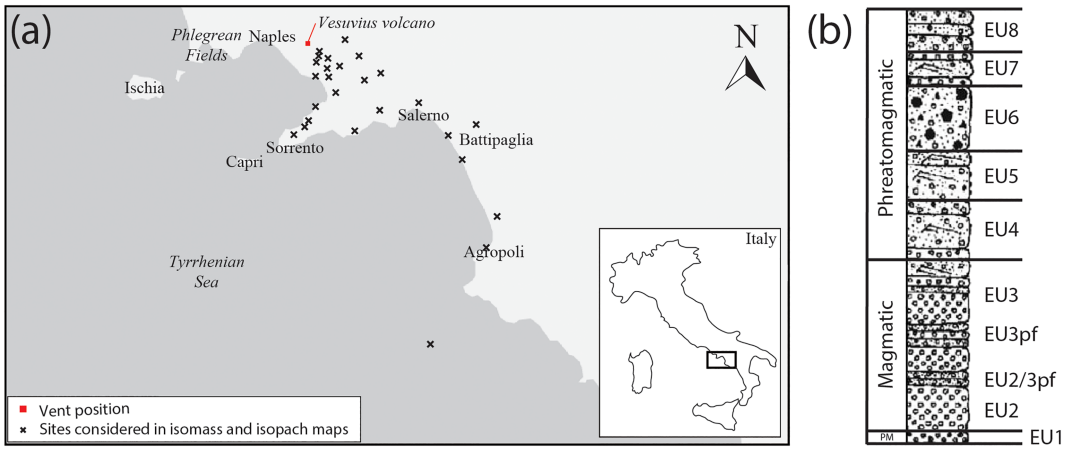

Figure 1. (a) Map of the Campanian region (Italy) including the Vesuvius volcano position. (b) Stratigraphy of the deposits of the 79 CE eruption. Modified from Gurioli et al. (2005).

Among these, the 79 CE eruption was one of the most catastrophic volcanic events in the history, destroying the Roman towns of Herculaneum, Pompeii, and Stabiae (Sigurdsson et al., 1985). The eruptive sequence was divided into eight eruptive units (EU1-EU8) by Cioni, Sbrana, and Vecci (1992) and *Cioni* et al. (1995; Figure 1b). The eruption onset was characterized by a small phreatomagmatic explosion, with the deposition of a thin basal ash layer (EU1; Cioni, Sbrana, & Vecci, 1992; Cioni et al., 2000). This phase was followed by a Plinian phase which deposited a thick blanket of white phonolitic (EU2) and gray phono-tephritic (EU3) pumice (Lirer et al., 1973; Sigurdsson et al., 1990), interrupted by at least four pyroclastic currents (Cioni, Marianelli, & Sbrana, 1992; Sheridan et al., 1981). The Plinian phase was followed by a phase dominated by repeated pyroclastic current formation with minor fallout episodes (EU4 to EU8), and increasing contents of external water (Cioni, 2000). The transition from fall phases to pyroclastic currents was studied in detail by Shea et al. (2012), showing the incorporation of magma from the conduit margins as an efficient mechanism for increasing the proportion of dense pyroclasts in the erupted mixture. Further insights into the shift from a fully buoyant eruption plume to a collapsing column during the transition from EU3 to EU4 were provided by Neri et al. (2003), who also discussed the effect of microlite content in controlling magma viscosity and eventually eruptive dynamics.

EU2 is mainly composed by white pumice with sparse sanidine phenocrysts. At proximal and medial sites, this unit exhibits a symmetric gradation, with a reversely-graded base capped by a thin, normally-graded top. Using the maximum grain size level as an isochronal marker, two sub-units were defined: EU2a and EU2b. At some proximal sites, a thin, whitish to gray, ash layer marks the transition between EU2 and EU3 (Cioni, Marianelli, & Sbrana, 1992). EU3 gray pumice is richer in phenocrysts (mainly clinopyroxene and sanidine) and microlites (mainly leucite) with respect to the EU2 white pumice, and the deposit exhibits a larger dispersal area and a generally coarser grain size. Several pyroclastic current deposits are intercalated with EU3, which, like EU2, presents a symmetric gradation, with a reversely-graded base and a normally-graded top. Also in this case, the maximum grain size level represents an isochronal marker, allowing to define two sublevels: EU3a and EU3b. Because deposits in the proximal sites were affected by the erosive effects of pyroclastic currents, the symmetric grading is more evident in the medial and sometimes distal sections. Above these fallout deposits, pyroclastic current deposits prevail, representing the end of the Plinian phase and marking the caldera collapse (Cioni et al., 1999; Shea et al., 2011).

The lithic fragments are composed by lavas, limestones, marbles, and scarce skarns and cumulate rocks (detailed information associated with the different components identified in this eruption can be found in Cioni et al., 1995). Lithic fragments have variable abundance in the different subunits of the fallout deposit, with lava fragments being always predominant, and carbonates (i.e., limestone and marbles) occurring mainly in EU3.

3. Methods

3.1. Lithic Fragments Data

3.1.1. Sampling and Complementary Information

In order to characterize the fallout deposits of EU2 and EU3, the following measures were taken at 22 sampling sites: (1) total thickness and (2) thickness of the four subunits defined here. Additionally, bulk samples were collected along all the subunits in order to characterize the grain size distribution, density, and componentry (Table S1 in the supporting information). Published information was included in the studied dataset, considering thickness data of some additional sites, for the whole deposit, EU2, and EU3 (Table S1; Carey & Sigurdsson, 1987).

3.1.2. Sample Analysis

Samples were dried and then the bulk density of some selected samples was measured, assuming to obtain a representative value of the deposit density. For that, the weight of each sample was measured, and samples were then poured into a graduated cylinder and gently tapped five times, before measuring the volume. This procedure was repeated three times for each sample, and the different measures averaged. In order to study the grain size distribution of the collected samples, samples were mechanically sieved between $\phi = -5$ and $\phi = +4$, where $\phi = -\log_2(D/D_0)$, D is pyroclast diameter, and $D_0 = 1$ mm. Additionally, samples were split into six groups: (1) pumice, (2) limestone and dolostone, (3) marble, (4) loose crystals, (5) cumulate and skarn rocks, and (6) other intrusives, using the granulometric classes with $\phi \leq 0$ (please note that cumulate and skarn rocks are grouped in the same class because they are interpreted as part of the magma chamber walls; Cioni et al., 1995). The mass fraction of each class for each sampling site and subunit was then calculated using the grain size distributions, and finally, thickness and density data were used to compute the mass per unit area of each component for each sampling site and subunit (Tables S2–S4).

3.1.3. Isomaps

Based on our stratigraphic data and literature-derived information, we traced isopach and isomass maps of the following levels: EU2, EU2a, EU2b, EU3, EU3a, and EU3b. The main uncertainty sources of this procedure derive from the irregular distribution of the sampling sites, which is mainly a consequence of the deposition in the sea of the western portion of the dispersal lobe, and from the occurrence of significant erosion of the proximal deposits by pyroclastic currents (Cioni et al., 2000; Cioni, Marianelli, & Sbrana, 1992). Furthermore, based on the grain size distribution and componentry analysis, we traced additional isomass maps of the studied subunits for specific components: pumice, loose crystals, total lithic fragments, lavas, and carbonates. From these results and using different estimation methods (exponential with one and two segments, Weibull, and power law-based estimates; Table S5; Pyle, 1989; Bonadonna & Costa, 2012), we calculated the total mass of the different types of lithic fragments (M_{li} and M_{ci} for lavas and carbonates, respectively) ejected during the different phases of the eruption. Mass estimates were then converted to volume (V_{li} and V_{ci} for lavas and carbonates, respectively) using a reference lithic fragments density (ρ_{lf}).

3.2. Numerical Modeling

3.2.1. Steady-State Model

In order to study the eruptive dynamics of the 79 CE Vesuvius eruption, we use the 1D-steady state model (http://demichie.github.io/MAMMA) presented by de' Michieli Vitturi et al. (2011) and La Spina et al. (2015). The model is capable of describing the evolution of magma properties along the conduit (e.g., velocity, pressure, and density), accounts for the most important processes acting on ascending magmas (e.g., rheological changes, fragmentation, crystallization), and allows consideration of conduits with depth-dependent dimensions (Text S1). We selected an appropriate set of constitutive equations for describing magma rheology, crystallization, water exsolution, outgassing, and the equations of state for this specific case study (Table 1), and additional parameters were calibrated using literature data: magma crystallinity, critical volume fraction of exsolved gas for magma fragmentation, and bubble number density (Table 2). We considered the emission of two different magma compositions throughout the eruption (phonolite and tephritic phonolite; Table 2), with different rheologies (Giordano et al., 2008). Finally, we assumed that magma chamber overpressure is a linear function of the erupted mass, and varies between two arbitrary limits: +20 and −40 MPa. This wide range was selected by considering the caldera-forming character of the eruption, which would require a significant pressure drop in the magma reservoir (Marti et al., 2000) and is consistent with the pressure variation assumed by Massaro et al. (2018) for a similar Plinian eruption of SVVC.

Table 1
Constitutive Equations Used in Conduit Simulations

Parameter	Model
Viscosity model	Giordano et al. (2008)
Crystallinity model	de' Michieli Vitturi et al. (2010)
Influence of crystals on viscosity	Costa (2005)
Influence of bubbles on viscosity	Costa et al. (2007)
Solubility model	Polynomial fit[a]
Outgassing model	Forchheimer's law[b]
Exsolved gas equation of state	Ideal gas
Equation of state of melt, crystals and dissolved gas	Mie-Grüneisen[c]

Note. Additional information is presented in Table S9.
[a]Based on Carroll and Blank (1997). [b]Degruyter et al. (2012). [c]Le Métayer et al. (2005).

3.2.2. Conduit Geometry

Based on crystallization experiments, phenocryst assemblage, and the study of melt inclusions, Scaillet et al. (2008) suggested that the reservoir that fed the 79 CE Vesuvius eruption was located at 7- to 8-km depth. Thus, in this work we assumed a magma reservoir depth (L) of 8,000 m, and we also considered that the limit between lavas and carbonates (h_{cl}) in the central part of the caldera is located at 2,300-m depth (i.e., h_{cl} = 5,700 m) (Balducci et al., 1985; Bernasconi et al., 1981; Brocchini et al., 2001). Based on the expected erosion processes in explosive eruptions (Aravena et al., 2017; Macedonio et al., 1994), we considered three different geometric configurations whose dimensions are variable during the eruption: (1) cylindrical conduit (type C, Figure 2a), (2) two coaxial cylindrical portions connected by an axisymmetric transitional zone (type NC2, Figure 2b), and (3) cylindrical conduit in deep domains with an axisymmetric, shallower portion of upward linear enlarging (type NC3; Figure 2c). All these geometric configurations are then connected to the surface through a crater area (an inverted truncated cone), whose deeper cross section represents the upper boundary of the conduit for numerical modeling. It is worth highlighting that a dyke-like geometry for the conduit is likely to characterize the initial part of an eruption, when rock fracture is the process that dominates the onset of magma ascent, eventually influenced by the existence of previous conduit systems. However, as the model used for conduit simulations is steady-state and we did not consider the opening phase of the eruption, this transient phase does not represent the focus of our simulations. Indeed, as evidenced in several natural cases (Fink, 1985; Quareni et al., 2001), dyke-like geometry rapidly shifts to a focused flow along one or more points of the fracture, thus developing cylinder-like conduits. We assume here that this geometry can be considered dominant under fully-developed steady-state conditions.

Table 2
Fixed Input Parameters Used in Conduit Simulations

Magma composition	White magma (Phonolite)	Gray magma (Tephritic phonolite)	
Subunit	EU2	EU3a	EU3b
SiO_2 (wt. %)	56.71	54.73	54.73
TiO_2 (wt. %)	0.21	0.54	0.54
Al_2O_3 (wt. %)	21.17	19.36	19.36
Fe_2O_3(t) (wt. %)	2.44	4.60	4.60
MnO (wt. %)	0.13	0.14	0.14
MgO (wt. %)	0.42	1.60	1.60
CaO (wt. %)	2.81	5.35	5.35
Na_2O (wt. %)	6.35	4.49	4.49
K_2O (wt. %)	9.75	9.04	9.04
P_2O_5 (wt. %)	0.02	0.18	0.18
Temperature (°C)	850	950	950
Water content (wt. %)	6.0	4.0	4.0
Crystallinity at conduit bottom (vol. %)	9	10	8
Maximum crystallinity (vol. %)	39	52	53
Critical fraction of exsolved gas (vol. %)	77.9	62.0	69.2
Bubble number density (mm^{-3})	3.0×10^6	6.6×10^5	2.5×10^6

Note. Macedonio et al. (1994), Cioni et al. (1995), and Gurioli et al. (2005).

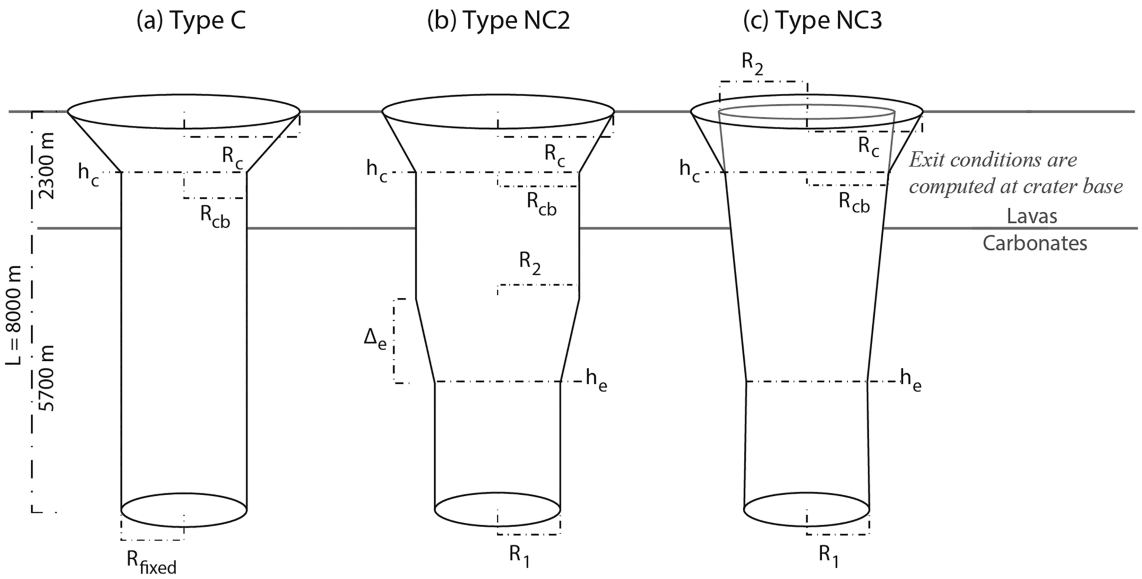

Figure 2. (a) Cylindrical conduit. (b) Two coaxial cylindrical portions connected by a transitional zone. (c) Cylindrical conduit in deep domains with a shallower portion of upward linear enlarging. All these geometric configurations are then connected to the surface through a crater zone. h_c is crater bottom position, R_{cb} is conduit radius at crater bottom, R_c is crater radius, and R_{fixed}, R_1, R_2, h_e, and $_e$ are the characteristic geometric parameters that define conduit geometry between its base and crater base (see Appendix A1).

Considering field data-based geometrical constraints (in particular, the volume of lavas and carbonates estimated in the pyroclastic deposits of each eruptive unit; Appendix A1), for the three geometric configurations considered as representative of likely volcanic conduits (i.e., types C, NC2, and NC3), we obtained a set of geometric parameters compatible with the volume of the different types of lithic fragments eroded from the conduit during each phase of the studied eruption. For type C geometric configuration, only one conduit geometry, characterized by specific values of R_{fixed}, R_c, and h_c (Figure 2a), is able to satisfy a given estimate of the volume and type of lithic fragments, where R_{fixed} is conduit radius, R_c is crater radius, and h_c is the distance between conduit base and crater bottom. For types NC2 and NC3, an infinite group of conduit geometries is consistent with a given estimate of the eroded volume and type of lithic fragments, and each one of them is fully characterized by two geometric parameters: h_e and R_2 (i.e., the other geometric parameters can be unequivocally calculated for known values of h_e and R_2, see Appendix A1), where h_e is the distance between conduit base and the position of conduit enlargement for geometric configurations NC2 and NC3, and R_2 is a characteristic radius that defines the magnitude of conduit enlargement for geometric configurations NC2 and NC3 (Figures 2b and 2c).

In addition to the estimates of the volume of lithic fragments, conduit geometry is expected to be able to produce modeling results consistent with two other conditions: (1) the MDR of each phase of the eruption (MDR_e), where we use published information (Carey & Sigurdsson, 1987; see section 4.1); and (2) the position of the fragmentation level, which should be located slightly above h_e (see Figures 2b and 2c and Appendix A1). This latter condition is the only way to reasonably make a given conduit geometry with depth-variable dimensions by considering a mechanical stability-based approach, because the erosion processes are expected to be more intense near and above the fragmentation level due to the likely occurrence of collapse processes and the effect of pyroclast impact (Aravena et al., 2017; Macedonio et al., 1994).

Using conduit geometries compatible with the volume of the different types of lithic fragments eroded from the conduit, we developed a set of numerical simulations of magma ascent and then we evaluated their output parameters through the analysis of the degree of agreement of the simulated MDR and fragmentation level, which was performed by considering appropriate mathematical expressions (see Appendix A1). In this way, we can determine the set of conduit geometric parameters that best fit the prescribed MDR and the expected fragmentation level, and thus we can propose the temporal evolution of conduit geometry and other key eruptive parameters. Here we study the conduit evolution during three stages of the Plinian

Table 3
Summary of Masses and Volumes of the Studied Subunits, Calculated From the Isomass and Isopach Maps

Unit/Subunit	EU2	EU3	EU2a	EU2b	EU3a	EU3b
Total volume (m^3)	$8.7{\cdot}10^8$	$1.3{\cdot}10^9$	$6.6{\cdot}10^8$	$2.1{\cdot}10^8$	$2.7{\cdot}10^8$	$1.1{\cdot}10^9$
Total mass (kg)	$6.1{\cdot}10^{11}$	$1.0{\cdot}10^{12}$	$4.7{\cdot}10^{11}$	$1.4{\cdot}10^{11}$	$1.9{\cdot}10^{11}$	$8.3{\cdot}10^{11}$
Pumice (kg)			$3.5{\cdot}10^{11}$	$1.1{\cdot}10^{11}$	$1.5{\cdot}10^{11}$	$5.8{\cdot}10^{11}$
Crystals (kg)			$5.4{\cdot}10^{10}$	$1.6{\cdot}10^9$	$7.1{\cdot}10^9$	$8.4{\cdot}10^{10}$
Lithics (kg)			$7.1{\cdot}10^{10}$	$2.6{\cdot}10^{10}$	$2.9{\cdot}10^{10}$	$1.6{\cdot}10^{11}$
Lavas (kg)			$5.7{\cdot}10^{10}$	$2.1{\cdot}10^{10}$	$2.1{\cdot}10^{10}$	$1.3{\cdot}10^{11}$
Mass fraction[a]			0.80	0.81	0.74	0.78
Carbonates (kg)			$1.4{\cdot}10^{10}$	$4.9{\cdot}10^9$	$7.7{\cdot}10^9$	$3.5{\cdot}10^{10}$
Mass fraction[a]			0.20	0.19	0.26	0.22

Note. Additional information is presented in Table S5.
[a]Calculated with respect to the total mass of lithics of each eruptive subunit.

phase of the 79 CE Vesuvius eruption (subunits EU2a, EU3a, and EU3b). The reason for disregarding EU2b is explained in section 4.1.

4. Results

4.1. Erupted Mass, Erupted Volume, and Mass Discharge Rate

The masses and volumes of the studied units, subunits, and componentry classes, calculated from the isomass and isopach maps, are shown in Table 3 (more detailed information is presented in Figures S1–S6 and Tables S5–S8). It includes the mass of lithic fragments eroded from the conduit during each eruptive subunit, which were converted into volume using a reference density of 2,700 kg/m^3. These values contributed to the input parameters used in numerical simulations (Table 4).

Because the definition of the eruptive subunits considers different criteria than those employed by Carey and Sigurdsson (1987), some additional assumptions are necessary. Considering that the tops of EU2a and EU3a represent the levels with the maximum grain size of each eruptive unit, they likely record the maximum eruption rates. This is in agreement with the MDR evolution of EU3 presented by Carey and Sigurdsson (1987), but it is inconsistent with a monotonic increase of MDR during the emission of EU2 (Carey & Sigurdsson, 1987). Because the temporal evolution of MDR estimates is based on the analysis of height-normalized stratigraphic sections (Carey & Sigurdsson, 1987), they implicitly assume a constant dispersion area during the eruption, which is not in agreement with the results presented here. According to our results, >75% of the EU2 juvenile mass was emitted during EU2a, and thus an intermediate value of the last stages of subunit EU2 (Carey & Sigurdsson, 1987) seems to be a good approximation for the end of EU2a, whereas EU2b was not included in numerical simulations because of the lack of reliable information for constraining the MDR. The volume of lithic fragments eroded during EU2b was, however, added to the next phase considered in numerical simulations (i.e., EU3a). For the end of EU3a, we have employed the first sublevel of EU3 defined by *Carey and Sigurdsson* (1987; i.e., the peak of MDR), while EU3b represents an intermediate value of the remaining sublevels. In this sense, although the last value of MDR of EU3 (Carey & Sigurdsson, 1987) could be considered the most appropriate estimate for the end of EU3b, the occurrence of large pyroclastic currents during the final stages of EU3 (Cioni, 2000; Shea et al., 2011) is expected to produce an important reduction in column height-based estimates of MDR. The adopted values of MDR during the eruption, which are expected to be representative of the last stages of each eruptive phase, are presented in Table 4 and graphically described in Figure S7. We remark that a significant uncertainty is associated with these estimates of MDR (Carey & Sigurdsson, 1987), which are based on a procedure that assumes a very simplified plume dynamics and poorly-constrained meteorological conditions. Because our procedure is strongly controlled by the MDR estimates, this likely propagates in a relevant uncertainty in the numerical results presented here. It is also important to stress that MDR is not an input parameter in magma ascent simulations but an output, which is employed to assess the degree of agreement of the modeled MDR with respect to the estimated value for the different phases of the eruption (Carey & Sigurdsson, 1987).

Table 4
Isomass Maps-Derived Input Parameters Used in Numerical Simulations

Subunit	EU2a	EU3a[a]	EU3b
Volume of lavas eroded from the conduit (V_{li}; m^3)	$2.1{\cdot}10^7$	$1.6{\cdot}10^7$	$4.6{\cdot}10^7$
Volume of carbonatic fragments eroded from the conduit (V_{ci}; m^3)	$5.2{\cdot}10^6$	$4.6{\cdot}10^6$	$1.3{\cdot}10^7$
MDR_e (kg/s)	$6.0{\cdot}10^7$	$1.5{\cdot}10^8$	$8.0{\cdot}10^7$
Inlet overpressure (MPa)	+2.6	−10.6	−40.0

Note. The MDR of each subunit is also reported (Carey & Sigurdsson, 1987). The graphical representation of the MDR of each subunit is presented in Figure S7.
Abbreviation: MDR: mass discharge rate.
[a]The volume of lithics also includes the lithics ejected during EU2b.

The density of pyroclastic deposits varies between about ~660 and ~780 kg/m^3, with values sensibly higher for those units with a larger dispersion (i.e., EU2a and EU3b). This is a consequence of the higher densities typically measured at distal sampling sites. The mass fraction of lithic fragments varies between 15% and 19%, with higher values for the two upper units (i.e., EU2b and EU3b). The proportion of carbonates in the lithic component is consistent with Macedonio et al. (1994), exhibiting higher values for EU3 and varying between 0.19 and 0.26.

4.2. Temporal Evolution of Conduit Geometry

Field data-derived information on the erupted mass, volume of the different types of lithic fragments, and literature-derived information of the MDR evolution and subsurface stratigraphy were used to constrain the evolution of conduit geometry in the course of the eruption. Modeling results associated with the different geometric configurations considered here are discussed below (Table 5 and Figures 3–5).

4.2.1. Geometric Configuration C

Table 5 presents the results derived from the assumption of an erosion process characterized by the generation of conduits with fixed dimensions in depth, considering the three phases of the 79 CE Vesuvius eruption addressed in this work. Results indicate that cylindrical conduits are not capable of producing consistent values with the 79 CE Vesuvius eruption. In particular, numerical modeling predicts an important increase in MDR between EU3a and EU3b (from $1.6{\cdot}10^8$ kg/s to $2.7{\cdot}10^8$ kg/s, Table 5) as a consequence of an abrupt conduit radius increase (from ~23 to ~36 m), which is highly inconsistent with literature data (Table 4).

4.2.2. Geometric Configuration NC2

4.2.2.1. Phase EU2a

Considering the geometric configuration NC2, the most probable conduit geometry fitting the data at the end of phase EU2a is characterized by a deep portion with a radius of ~17 m and a shallower portion with a radius of ~35 m, with the bottom of the enlargement zone at 2,450-m depth (h_e equal to 5,550 m, Figures 3a–3c). Consequently, the fragmentation level would have been located at 2,300-m depth, around the limit between carbonates and lavas. This geometry is associated with a crater radius of ~195 m and a crater depth of ~280 m (Figures 5a–5e), implying that crater excavation would have produced ~47% of the total mass of lithic fragments eroded during the ejection of EU2a.

Table 5
Results Associated With Cylindrical Conduit Simulations

Subunit	EU2a	EU3a	EU3b
Conduit radius (R_{fixed}; m)	17	23	36
Crater radius (m)	220	265	350
Crater depth (m)	350	420	540
MDR (kg/s)	$4.3{\cdot}10^7$	$1.6{\cdot}10^8$	$2.7{\cdot}10^8$
Fragmentation depth (m)	1440	760	1030
Exit pressure (MPa)	6.4	10.5	7.5
Exit velocity (m/s)	185	177	170

4.2.2.2. Phase EU3a

At the end of phase EU3a, conduit geometry would have been characterized by a deep portion with a radius of ~23 m and a shallower portion with a radius of ~55 m (Figures 3d–3f). The conduit dynamics would have produced a slightly shallower fragmentation level than the previous phase (2,250-m depth, that is, h_e equal to 5,600 m). In this case, crater excavation was less significant, producing ~24% of the total mass of lithic fragments eroded during the emission of this subunit, resulting in a crater radius and depth very similar to those of phase EU2a (~220 and ~280 m, respectively).

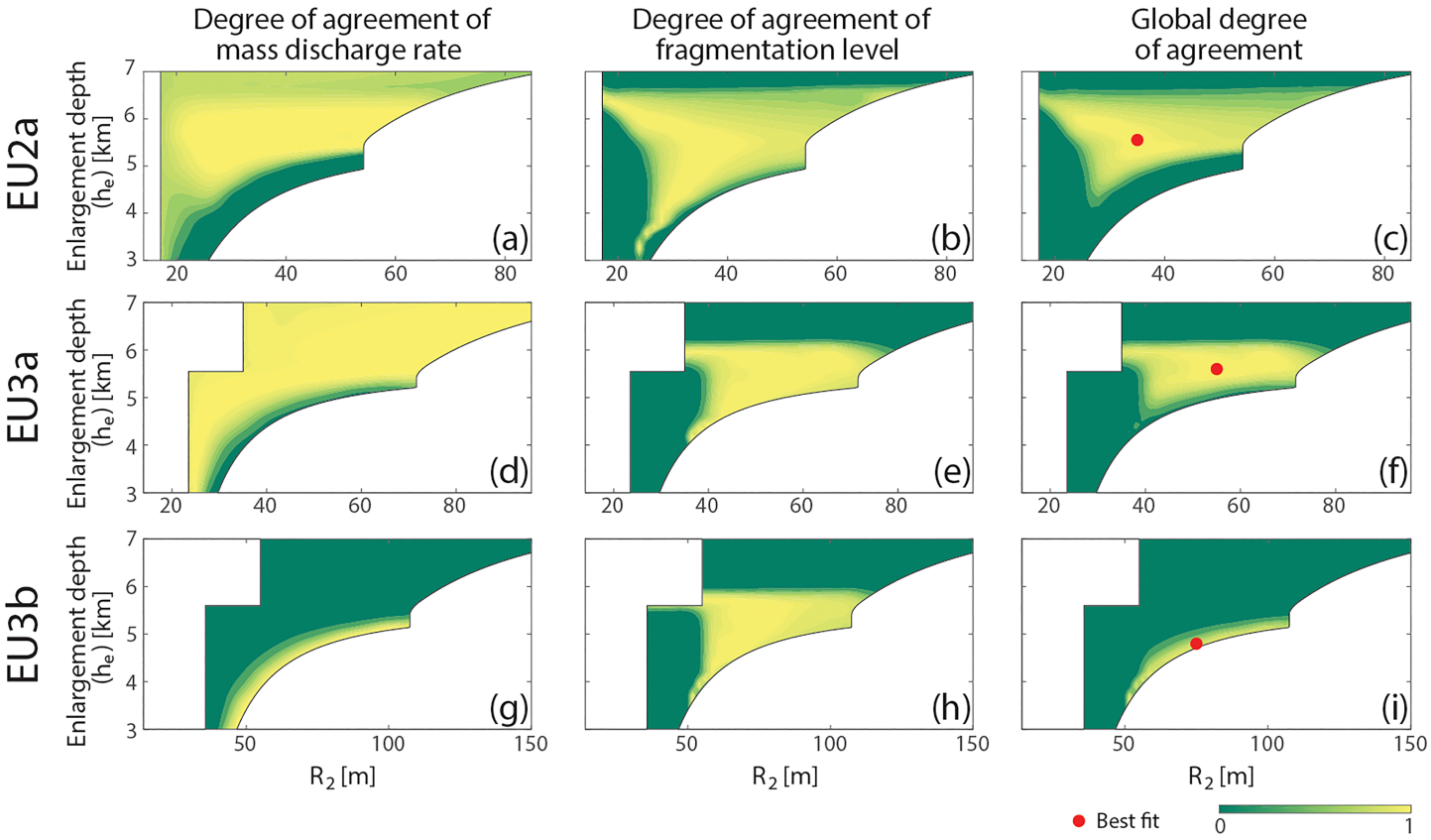

Figure 3. Contour plots of the parameters measuring the degree of agreement of mass discharge rate and fragmentation level, for (a–c) the end of phase EU2a, (d–f) the end of phase EU3a, and (g–i) the end of phase EU3b. These results are related to the use of geometric configuration NC2 for modeling the evolution of conduit geometry during the 79 CE Vesuvius eruption. The external white zone represents incompatible geometries with the volume of lithic fragments eroded from the conduit. The parameters adopted to measure the degree of agreement between numerical results, mass discharge rate estimates and the expected fragmentation level vary between 0 and 1, where 1 represents perfect agreement and 0 represents null agreement (see Appendix A1).

4.2.2.3. Phase EU3b

Results indicate that the most probable conduit geometry at the end of phase EU3b was characterized by a deep portion with a radius of ~25 m and a shallower portion with a radius of ~70 m (Figures 3g–3i). Additionally, fragmentation level was located at 3,050-m depth (h_e equal to 4,800 m), much deeper than the previous phases of the eruption. Significant crater excavation is estimated for this phase, representing ~50% of the total volume of lithic fragments eroded during the emission of this subunit. This process is associated with a crater radius and depth of ~305 and ~395 m, respectively.

Figure 5a presents a summary of the temporal evolution of conduit geometry, whereas Figures 5b–5e presents the evolution of key eruptive parameters. Exit velocity (i.e., erupted mixture velocity at crater base) experienced an abrupt decrease between EU2a and EU3a, mainly as a consequence of the lower water content of the tephri-phonolitic magma of gray pumices. Conversely, the transition from EU3a to EU3b was characterized by an abrupt drop in exit pressure (i.e., erupted mixture pressure at crater base) and only minor changes in exit velocity.

4.2.3. Geometric Configuration NC3

4.2.3.1. Phase EU2a

During the end of phase EU2a, the most probable geometry was characterized by a deep portion with a radius of ~17 m and an enlargement zone starting at 2,400-m depth (R_2 around 70 m; Figures 4a–4c). This condition is associated with a fragmentation level located at 2,100-m depth. This conduit geometry involves the presence of a crater radius of ~165 m, implying that crater excavation would have produced ~20% of the total mass of lithic fragments eroded from the conduit during EU2a, significantly lower than that predicted with geometric configuration NC2.

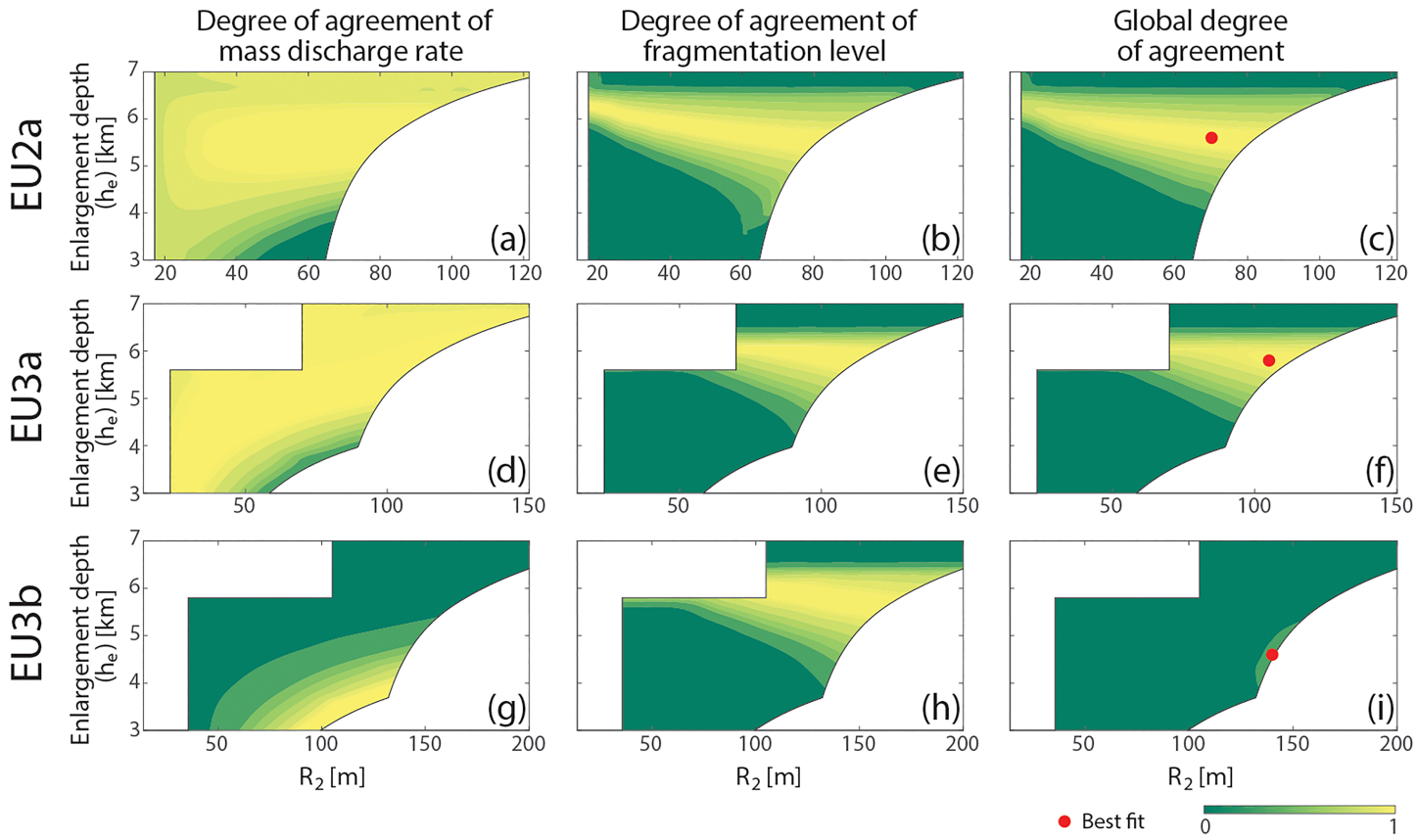

Figure 4. Contour plots of the parameters measuring the degree of agreement of mass discharge rate and fragmentation level, for (a–c) the end of phase EU2a, (d–f) the end of phase EU3a, and (g–i) the end of phase EU3b. These results are related to the use of geometric configuration NC3 for modeling the evolution of conduit geometry during the 79 CE Vesuvius eruption. The external white zone represents incompatible geometries with the volume of lithic fragments eroded from the conduit. The parameters adopted to measure the degree of agreement between numerical results, mass discharge rate estimates and the expected fragmentation level vary between 0 and 1, where 1 represents perfect agreement and 0 represents null agreement (see Appendix A1).

4.2.3.2. Phase EU3a

At the end of phase EU3a, conduit geometry would have been characterized by a deep portion with a radius of ~23 m and the bottom of the enlargement zone at 2,200-m depth (R_2 around 105 m; Figures 4d–4f). The water content decrease resulted in a shallower fragmentation level than that predicted for the end of phase EU2a (in this case, 1,900-m depth). Finally, weak crater excavation would have occurred during this phase (crater radius of ~185 m), representing ~10% of the lithic fragments eroded during the emission of EU3a.

4.2.3.3. Phase EU3b

For the end of this phase and considering geometric configuration NC3, the degree of agreement between numerical results, the estimated MDR and the expected fragmentation depth is sensibly lower than that obtained for geometric configuration NC2 and for the previous phases of the eruption, and unrealistic values of Δ_f (e.g., >600 m) are required for obtaining a satisfactory degree of agreement (i.e., a global degree of agreement near 1.0, see Appendix A1). Still, numerical simulations indicate that the most probable conduit geometry was characterized by a deep portion with a radius of ~31 m and an enlargement domain starting very deep, at 3,400-m depth (R_2 around 140 m; Figures 4g–4i). Fragmentation level is much deeper than the obtained for previous phases (depth of 3,100 m), which is consistent with the results derived from the use of geometric configuration NC2. In this case, in contrast to the results obtained with geometric configuration NC2, weak crater excavation is expected to have occurred during this phase (~3% of the lithic fragments eroded during the emission of EU3b are associated with crater excavation, with a crater radius of ~200 m).

Figure 5f exhibits a summary of the temporal evolution of conduit geometry for geometric configuration NC3, whereas Figures 5g–5j present the evolution of fragmentation depth, exit pressure, exit velocity, and

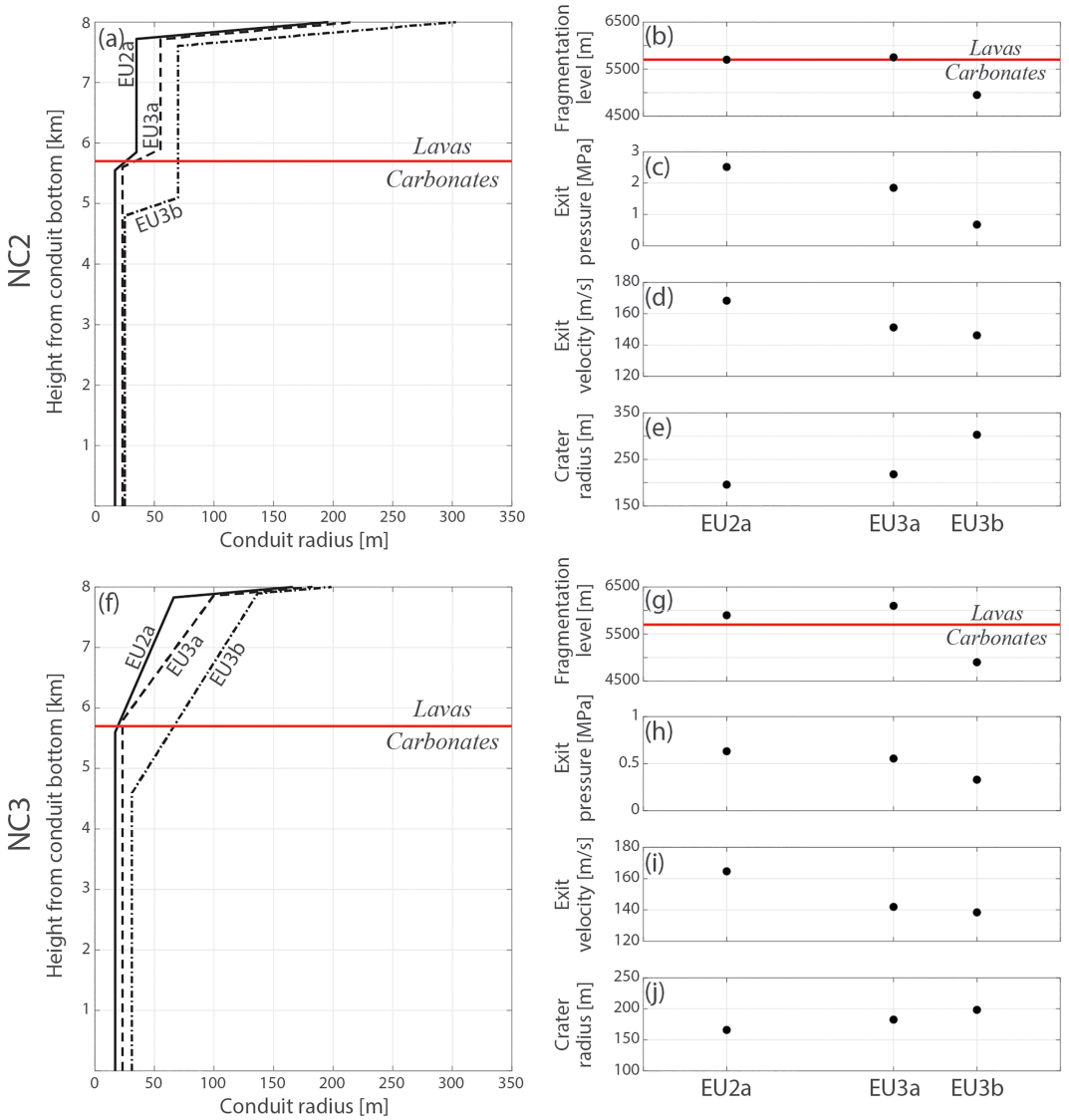

Figure 5. Temporal evolution of conduit geometry, fragmentation depth, exit pressure, exit velocity, and crater radius during the 79 CE Vesuvius eruption, using geometric configurations (a–e) NC2 and (f–j) NC3.

crater radius during the eruption. Although geometric configuration NC3 is characterized by much lower exit pressures (Figures 5c and 5h), results produce very similar trends of temporal evolution for fragmentation level, exit pressure and exit velocity for both geometric configurations with depth-variable dimensions (Figures 5c and 5d and 5h and 5i for comparisons).

5. Discussion

Based on the analysis of the volume and type of lithic fragments eroded from the conduit during the 79 CE Vesuvius eruption and their use as inputs of conduit models, we reconstructed the temporal evolution of this eruption, constraining key characteristics such as conduit geometry, crater dimensions, exit pressure, and exit velocity.

Two feasible geometric configurations with depth-dependent dimensions were tested in this work (types NC2 and NC3, see Figures 2b and 2c). They exhibit reasonably consistent results, and are capable of reconstructing the temporal evolution of the 79 CE Vesuvius eruption. Geometric configuration NC2 shows a better performance than geometric configuration NC3, whereas modeling results for fixed diameter,

cylindrical conduits (type C, see Figure 2a) are not consistent with the eruptive dynamics of the eruption. Indeed, in general, it seems difficult to reproduce the waning stages of explosive eruptions with a cylindrical conduit enlarging with time, at least for realistic decreases of inlet pressure (e.g., <80 MPa).

Numerical simulations indicate that the abrupt increase of MDR between the first stage of the Plinian phase (i.e., EU2a) and the peak of MDR (i.e., EU3a) was the product of a particularly efficient increase of conduit dimensions in deep domains, which tended to produce almost cylindrical geometries in the carbonate zone and counterbalanced the MDR-decreasing effect produced by the progressive depressurization of the magma reservoir. During these phases, the magma fragmentation depth experienced slight modifications, and was located near the limit between carbonates and lavas. Conduit erosion during the emission of EU3b produced slight changes in the conduit radius in deep domains and significant enlargement tendencies in the upper portion of the carbonatic basement, which required the occurrence of deep magma fragmentation (>3 km depth for both geometric configurations with depth-variable dimensions). This process, along with an abrupt inlet pressure drop, was manifested in a general decrease of MDR.

Results suggest that the increase of crater dimensions was particularly intense during the initial stages of the Plinian phase of the eruption (i.e., EU2a), reaching quickly a crater radius larger than 150 m (in particular, at the end of phase EU2a, ~195 and ~165 m for simulations associated with geometric configurations NC2 and NC3, respectively). Between the end of EU2a and the peak of MDR (i.e., the end of EU3a), a stabilization of crater dimensions is suggested by our simulations, with a relative variation in crater radius lower than 10%. In fact, the fraction of lithic fragments injected by crater excavation in the eruptive mixture drops from ~47% to ~24% between the phases EU2a and EU3a when NC2-type geometries are considered; and from ~20% to ~10% when NC3-type geometries are adopted. A new intensification of crater excavation processes is predicted during the emission of EU3b, which may have announced the occurrence of important conduit collapses favored by a significant deepening of the fragmentation level. Because a significant part of the eroded lithic fragments may come from crater excavation processes (lava fragments), our results suggest that crater excavation represents a critical process to consider in the reconstruction of conduit geometry through the use of the volume and type of lithic fragments. We highlight that these modifications in the intensity of crater excavation and fragmentation depth are not manifested in dramatic changes in the fraction of lithic fragments in pyroclastic deposits, and the increase in the ratio between carbonates and lavas between EU2 and EU3 is only moderate.

Exit pressure and exit velocity would have experienced a monotonically decreasing tendency during all the Plinian phase, mainly conditioned by the decrease in water content between EU2a and EU3a and the abrupt increase in the conduit radius in shallow domains between EU3a and EU3b. This tendency is consistent with a shift of the eruptive dynamics from a convective plume to a collapsing column, as described for the studied eruption (Carey & Sigurdsson, 1987; Cioni et al., 1999).

6. Concluding Remarks

The volume and type of lithic fragments erupted during an explosive event can be successfully employed to reconstruct the temporal evolution of past volcanic eruptions, constraining different parameters such as conduit geometry, crater dimensions, exit pressure, and exit velocity. The presence of several sources of information is required for this type of reconstruction:

a The volume of lithic fragments, which derives from field data. An appropriate procedure for calculating it includes measures of thickness of pyroclastic deposits, density, grain size distribution, and componentry; the design of isopach and isomass maps; and the application of appropriate methods for estimating the total mass of each component in the pyroclastic deposits.
b Additional information for constraining the input parameters and constitutive equations used in numerical simulations and for setting other features of the eruption. In this case, we use the MDR, but any well-constrained eruptive parameter can be useful for these purposes (e.g., exit velocity, exit pressure).

We reconstructed the temporal evolution of the Plinian phase of the 79 CE Vesuvius eruption. We showed that only conduits with depth-dependent dimensions can reproduce a temporal evolution consistent with the dynamics of the studied eruption. Results suggest that the onset of the Plinian phase was characterized by intense crater excavation processes. The increase in MDR during the transition between EU2 and EU3

coincided with an efficient increase of conduit diameter at depth and, after the peak of MDR, a significant deepening of the fragmentation level and an abrupt inlet pressure drop would have occurred, manifested in the decreasing MDR. Exit pressure and exit velocity would have experienced a monotonic decreasing tendency during all the Plinian phase, consistent with the shift to collapsing columns and pyroclastic currents observed in this eruption.

Appendix A1

The expressions adopted to describe the geometric configurations C, NC2, and NC3 (Figure 2) are:

$$\mathrm{R}(h) = \begin{cases} R_{\text{fixed}} & if\ h \le h_c \\ R_{cb} + \phi_c(h - h_c) & if\ h > h_c \end{cases} \tag{1}$$

$$R(h) = \begin{cases} R_1 & if\ h \le h_e \\ R_1 + \phi_1(h - h_e) & if\ h_e < h \le h_e + \Delta_e \\ R_2 & if\ h_e + \Delta_e < h \le h_c \\ R_{cb} + \phi_c(h - h_c) & if\ h > h_c \end{cases} \tag{2}$$

$$R(h) = \begin{cases} R_1 & if\ h \le h_e \\ R_1 + \phi_2(h - h_e) & if\ h_e < h \le h_c \\ R_{cb} + \phi_c(h - h_c) & if\ h > h_c \end{cases} \tag{3}$$

where $R(h)$ is conduit radius as a function of the height h ($h = 0$ is conduit bottom, and $h = L$ represents the surface), R_{fixed}, R_1, R_2, and R_c are the characteristic dimensions of the conduit for the different geometric configurations, h_e is the height of the enlarging zone bottom in NC2-type and NC3-type conduits, h_c is the height of the crater bottom, Δ_e is the length of the transitional zone in NC2-type conduits, $\phi_1 = (R_2 - R_1)/\Delta_e$, $\phi_2 = (R_2 - R_1)/(L - h_e)$, ϕ_c measures the crater angle (here assumed to produce a crater slope of 60°, Table S10; Moon et al., 2005), and R_{cb} is conduit radius at crater bottom and it is computed in order to satisfy the continuity of R(h) when $h = h_c$ (Figure 2).

Given the volume of lithic fragments (lavas and carbonates) eroded from the conduit during subunit i, we can constrain its geometric parameters:

a The volume of carbonates eroded for producing a given conduit geometry must be equal to the volume of carbonatic fragments calculated from field data (Table 3).
b The volume of lavas eroded to produce a given conduit geometry must be equal to the volume of lava fragments estimated from field data (Table 3).

These constraints result in:

$$V_{ci} = \frac{M_{ci}}{\rho_{lf}} = \int_{z=0}^{z=h_{cl}} \pi \cdot \left(R_e^2(h) - R_i^2(h)\right) dz \tag{4}$$

$$V_{li} = \frac{M_{li}}{\rho_{lf}} = \int_{z=h_{cl}}^{z=L} \pi \cdot \left(R_e^2(h) - R_i^2(h)\right) dz \tag{5}$$

where $R_e(h) = \max(R(h), R_i(h))$ is the effective conduit radius as a function of height (i.e., considering the geometry inherited from the previous phases) and $R_i(h)$ is the inherited conduit radius as a function of height (i.e., estimated for the previous phase). Initially (i.e., for EU2a), because of the lack of reliable geometric constraints, we assumed that $R_i(h) = 0$, which is justified by the negligible volume of the pyroclastic deposits associated with EU1 in comparison with EU2 and EU3. Please note that V_{ci}, M_{ci}, ρ_{lf}, V_{li}, and M_{li} are known values for each eruptive subunit, derived from the analysis of field data (see Section 4.1 and Table 3).

For geometric configuration C and assuming that $h_{cl} < h_c$, we have that $V_{ci} = V_{ci}(R_{\text{fixed}})$ is a monotonic function of R_{fixed}, and only one conduit geometry is able to satisfy the condition related to the volume of carbonates eroded from the conduit (equation (4)). This geometry is associated with unequivocally defined

values of R_c and R_{cb} in order to satisfy the condition related to the eroded volume of lavas (equation (5)) and the continuity of $R(h)$.

On the other hand, for geometric configurations NC2 and NC3, we have two scenarios:

a The enlargement zone is located above the carbonates-lavas limit (i.e., $h_e > h_{cl}$): in this case, $V_{ci} = V_{ci}(R_1)$ is a monotonic function of R_1, and only one value of R_1 is compatible with the volume of carbonates derived from field data (equation (4); indeed, $R_1 = R_{fixed}$). Given fixed values for Δ_e and ϕ_c (Table S10), we developed a set of simulations with variable values of R_2 (between $R_{2i} = R_1$ and R_{2f}) and h_e (between $h_{ei_1} = h_{cl}$ and h_{ef_1}), where R_{2f} and h_{ef_1} are arbitrary iteration limits. It is worth stressing that each pair (R_2, h_e) is associated with unequivocally defined values of R_c and R_{cb} in order to satisfy the condition related to the volume of lavas eroded from the conduit (equation (5)) and the continuity of R(h).

b The enlargement zone is located below the carbonates-lavas limit (i.e., $h_e < h_{cl}$): in this case, given a fixed value of Δ_e, $V_{ci} = V_{ci}(R_1, R_2, h_e)$. For a given pair ($R_2$, h_e), $V_{ci} = V_{ci}(R_1)$ is a monotonic function of R_1, and we can calculate an only value of R_1 for satisfying the condition related to the volume of carbonates derived from field data (equation (4); in this case, $R_1 < R_{fixed}$). Therefore, we developed a set of simulations with variable values of h_e (between h_{ei_2} and $h_{ef_2} = h_{cl}$) and R_2 (between $R_{2i} = R_1$ and R_{2f}), where h_{ei_2} is an arbitrary iteration limit; while the corresponding value of R_1 can be unequivocally determined for each pair (R_2, h_e). Also in this case, each pair (R_2, h_e) is associated with unequivocally defined values of R_c and R_{cb} in order to satisfy the condition related to the volume of lavas eroded from the conduit (equation (5)) and the continuity of R(h).

For each simulation associated with geometric configurations NC2 and NC3, we evaluated the degree of agreement between numerical results, the estimated MDR (Carey & Sigurdsson, 1987), and the expected fragmentation level by using the following expressions:

$$\text{Degree of Agreement of MDR} = A_{MDR} = \exp\left(-0.5\cdot\left(\frac{\log_{10}(MDR_e)-\log_{10}(MDR_s)}{\sigma_a}\right)^2\right) \quad (6)$$

$$\text{Degree of Agreement of Fragmentation Level} = A_{FL} = \exp\left(-0.5\cdot\left(\frac{FL_s-h_e-\Delta_f}{\sigma_b}\right)^2\right) \quad (7)$$

where MDR_s is the simulated mass discharge rate, FL_s is the simulated fragmentation level (with respect to conduit base), σ_a and σ_b are constant tolerance values, and Δ_f is the height difference between the fragmentation level and the bottom of the enlarging zone of geometric configurations NC2 and NC3 (Figure 2). Because numerical simulations exhibit an abrupt pressure drop that starts some hundreds of meters below the fragmentation level, Δ_f should adopt values within that range. The global agreement degree (GA) is defined by:

$$GA = A_{MDR}\cdot A_{FL} \quad (8)$$

GA, A_{MDR}, and A_{FL} range between 0 and 1, where 1 represents perfect agreement and 0 represents null agreement. For clarity, a notation summary is presented in Table S10.

Acknowledgments
We acknowledge valuable comments and suggestions provided by the Editor, by Greg Valentine, and by an anonymous reviewer, which improved the content of this article. All new data included in this paper are available on the website: https://osf.io/mcnz7/.

References

Aravena, A., Cioni, R., de' Michieli Vitturi, M., & Neri, A. (2018). Conduit stability effects on intensity and steadiness of explosive eruptions. *Scientific Reports*, *8*(4125).

Aravena, A., de' Michieli Vitturi, M., Cioni, R., & Neri, A. (2017). Stability of volcanic conduits during explosive eruptions. *Journal of Volcanology and Geothermal Research*, *339*, 52–62.

Aravena, A., de' Michieli Vitturi, M., Cioni, R., & Neri, A. (2018). Physical constraints for effective magma-water interaction along volcanic conduits during silicic explosive eruptions. *Geology*, *46*(10), 867–870.

Balducci, S., Vaselli, M., & Verdiani, G. (1985). Exploration well in the «Ottaviano» Permit, Italy: Trecase 1, paper presented at International Seminar on the Results of EC Geothermal Energy Research, *3*.

Barberi, F., Cioni, R., Rosi, M., Santacroce, R., Sbrana, A., & Vecci, R. (1989). Magmatic and phreatomagmatic phases in explosive eruptions of Vesuvius as deduced by grain-size and component analysis of the pyroclastic deposits. *Journal of Volcanology and Geothermal Research*, *38*(3-4), 287–307.

Bernasconi, A., Bruni, P., Gorla, L., Principe, C., & Sbrana, A. (1981). Risultati preliminari dell'esplorazione geotermica profonda nell'area vulcanica del Somma-Vesuvio. *Rend. Soc. Geol. It*, *4*, 237–240.

Blundy, J., & Cashman, K. (2001). Ascent-driven crystallisation of dacite magmas at Mount St Helens, 1980–1986. *Contributions to Mineralogy and Petrology*, *140*(6), 631–650.
Bonadonna, C., & Costa, A. (2012). Estimating the volume of tephra deposits: a new simple strategy. *Geology*, *G32769*, 32761.
Brocchini, D., Principe, C., Castradori, D., Laurenzi, M., & Gorla, L. (2001). Quaternary evolution of the southern sector of the Campanian Plain and early Somma-Vesuvius activity: insights from the Trecase 1 well. *Mineralogy and Petrology*, *73*(1-3), 67–91.
Büttner, R., Dellino, P., Raue, H., Sonder, I., & Zimanowski, B. (2006). Stress-induced brittle fragmentation of magmatic melts: Theory and experiments. *Journal of Geophysical Research*, *111*, B08204. https://doi.org/10.1029/2005JB003958
Carey, S., Gardner, J., & Sigurdsson, H. (1995). The intensity and magnitude of Holocene plinian eruptions from Mount St. *Helens volcano, Journal of Volcanology and Geothermal Research*, *66*(1-4), 185–202.
Carey, S., & Sigurdsson, H. (1987). Temporal variations in column height and magma discharge rate during the 79 AD eruption of Vesuvius. *Geological Society of America Bulletin*, *99*(2), 303–314.
Carey, S., & Sigurdsson, H. (1989). The intensity of plinian eruptions. *Bulletin of Volcanology*, *51*(1), 28–40.
Carroll, M., & Blank, J. (1997). The solubility of H2O in phonolitic melts. *American Mineralogist*, *82*(5-6), 549–556.
Cashman, K. (1988). Crystallization of Mount St. Helens 1980–1986 dacite: A quantitative textural approach. *Bulletin of Volcanology*, *50*(3), 194–209.
Cioni, R. (2000). Volatile content and degassing processes in the AD 79 magma chamber at Vesuvius (Italy). *Contributions to Mineralogy and Petrology*, *140*(1), 40–54.
Cioni, R., Bertagnini, A., Santacroce, R., & Andronico, D. (2008). Explosive activity and eruption scenarios at Somma-Vesuvius (Italy): towards a new classification scheme. *Journal of Volcanology and Geothermal Research*, *178*(3), 331–346.
Cioni, R., Civetta, L., Marianelli, P., Metrich, N., Santacroce, R., & Sbrana, A. (1995). Compositional layering and syn-eruptive mixing of a periodically refilled shallow magma chamber: the AD 79 Plinian eruption of Vesuvius. *Journal of Petrology*, *36*(3), 739–776.
Cioni, R., Gurioli, L., Sbrana, A., & Vougioukalakis, G. (2000). Precursors to the Plinian eruptions of Thera (Late Bronze Age) and Vesuvius (AD 79): Data from archaeological areas. *Physics and Chemistry of the Earth, Part A: Solid Earth and Geodesy*, *25*(9-11), 719–724.
Cioni, R., Marianelli, P., & Sbrana, A. (1992). Dynamics of the AD 79 eruption: stratigraphic, sedimentologic and geochemical data on the successions of the Somma-Vesuvius southern sector. *Acta Vulcanologica*, *2*, 109–123.
Cioni, R., Pistolesi, M., Bertagnini, A., Bonadonna, C., Hoskuldsson, A., & Scateni, B. (2014). Insights into the dynamics and evolution of the 2010 Eyjafjallajökull summit eruption (Iceland) provided by volcanic ash textures. *Earth and Planetary Science Letters*, *394*, 111–123.
Cioni, R., Santacroce, R., & Sbrana, A. (1999). Pyroclastic deposits as a guide for reconstructing the multi-stage evolution of the Somma-Vesuvius Caldera. *Bulletin of Volcanology*, *61*(4), 207–222.
Cioni, R., Sbrana, A., & Vecci, R. (1992). Morphologic features of juvenile pyroclasts from magmatic and phreatomagmatic deposits of Vesuvius. *Journal of Volcanology and Geothermal Research*, *51*(1), 61–78.
Connor, C., Hill, B., Winfrey, B., Franklin, N., & Femina, P. C. L. (2001). Estimation of volcanic hazards from tephra fallout. *Natural Hazards Review*, *2*(1), 33–42.
Costa, A. (2005). Viscosity of high crystal content melts: dependence on solid fraction. *Geophysical Research Letters*, *32*, L22308. https://doi.org/10.1029/2005GL024303
Costa, A., Melnik, O., & Sparks, R. (2007). Controls of conduit geometry and wallrock elasticity on lava dome eruptions. *Earth and Planetary Science Letters*, *260*(1), 137–151.
de' Michieli Vitturi, M., Clarke, A., Neri, A., & Voight, B. (2010). Transient effects of magma ascent dynamics along a geometrically variable dome-feeding conduit. *Earth and Planetary Science Letters*, *295*(3), 541–553.
de' Michieli Vitturi, M., Clarke, A., Neri, A., & Voight, B. (2011). Assessing the influence of disequilibrium crystallization and degassing during magma ascent in effusive and explosive eruptions, paper presented at AGU Fall Meeting Abstracts.
Degruyter, W., Bachmann, O., Burgisser, A., & Manga, M. (2012). The effects of outgassing on the transition between effusive and explosive silicic eruptions. *Earth and Planetary Science Letters*, *349*, 161–170.
Di Renzo, V., Di Vito, M. A., Arienzo, I., Carandente, A., Civetta, L., D'Antonio, M., et al. (2007). Magmatic history of Somma–Vesuvius on the basis of new geochemical and isotopic data from a deep borehole (Camaldoli della Torre). *Journal of Petrology*, *48*(4), 753–784.
Doubik, P., & Hill, B. E. (1999). Magmatic and hydromagmatic conduit development during the 1975 Tolbachik eruption, Kamchatka, with implications for hazards assessment at Yucca Mountain, NV. *Journal of Volcanology and Geothermal Research*, *91*(1), 43–64.
Eichelberger, J., & Koch, F. (1979). Lithic fragments in the Bandelier Tuff, Jemez Mountains, New Mexico. *Journal of Volcanology and Geothermal Research*, *5*(1-2), 115–134.
Fink, J. H. (1985). Geometry of silicic dikes beneath the Inyo Domes, California. *Journal of Geophysical Research*, *90*(B13), 11,127–11,133.
Giordano, D., Russell, J., & Dingwell, D. (2008). Viscosity of magmatic liquids: a model. *Earth and Planetary Science Letters*, *271*(1), 123–134.
Gurioli, L., Houghton, B., Cashman, K., & Cioni, R. (2005). Complex changes in eruption dynamics during the 79 AD eruption of Vesuvius. *Bulletin of Volcanology*, *67*(2), 144–159.
Hammer, J., Cashman, K., Hoblitt, R., & Newman, S. (1999). Degassing and microlite crystallization during pre-climactic events of the 1991 eruption of Mt. Pinatubo, Philippines. *Bulletin of Volcanology*, *60*(5), 355–380.
Harp, A. G., & Valentine, G. A. (2015). Shallow plumbing and eruptive processes of a scoria cone built on steep terrain. *Journal of Volcanology and Geothermal Research*, *294*, 37–55.
Keating, G. N., Valentine, G. A., Krier, D. J., & Perry, F. V. (2008). Shallow plumbing systems for small-volume basaltic volcanoes. *Bulletin of Volcanology*, *70*(5), 563–582.
Klug, C., & Cashman, K. (1996). Permeability development in vesiculating magmas: implications for fragmentation. *Bulletin of Volcanology*, *58*(2-3), 87–100.
La Spina, G., Burton, M., & de' Michieli Vitturi, M. (2015). Temperature evolution during magma ascent in basaltic effusive eruptions: A numerical application to Stromboli volcano. *Earth and Planetary Science Letters*, *426*, 89–100.
Le Métayer, O., Massoni, J., & Saurel, R. (2005). Modelling evaporation fronts with reactive Riemann solvers. *Journal of Computational Physics*, *205*(2), 567–610.
Lirer, L., Pescatore, T., Booth, B., & Walker, G. P. (1973). Two plinian pumice-fall deposits from Somma-Vesuvius, Italy. *Geological Society of America Bulletin*, *84*(3), 759–772.
Macedonio, G., Costa, A., & Folch, A. (2008). Ash fallout scenarios at Vesuvius: numerical simulations and implications for hazard assessment. *Journal of Volcanology and Geothermal Research*, *178*(3), 366–377.
Macedonio, G., Costa, A., Scollo, S., & Neri, A. (2016). Effects of eruption source parameter variation and meteorological dataset on tephra fallout hazard assessment: example from Vesuvius (Italy). *Journal of Applied Volcanology*, *5*(1), 5.

Macedonio, G., Dobran, F., & Neri, A. (1994). Erosion processes in volcanic conduits and application to the AD 79 eruption of Vesuvius. *Earth and Planetary Science Letters*, *121*(1), 137–152.
Marti, J., Folch, A., Neri, A., & Macedonio, G. (2000). Pressure evolution during explosive caldera-forming eruptions. *Earth and Planetary Science Letters*, *175*(3), 275–287.
Massaro, S., Costa, A., & Sulpizio, R. (2018). Evolution of the magma feeding system during a Plinian eruption: The case of Pomici di Avellino eruption of Somma–Vesuvius. *Italy, Earth and Planetary Science Letters*, *482*, 545–555.
Moon, V., Bradshaw, J., Smith, R., & de Lange, W. (2005). Geotechnical characterisation of stratocone crater wall sequences, White Island Volcano, New Zealand. *Engineering Geology*, *81*(2), 146–178.
Neri, A., Aspinall, W. P., Cioni, R., Bertagnini, A., Baxter, P. J., Zuccaro, G., et al. (2008). Developing an event tree for probabilistic hazard and risk assessment at Vesuvius. *Journal of Volcanology and Geothermal Research*, *178*(3), 397–415.
Neri, A., Papale, P., Del Seppia, D., & Santacroce, R. (2003). Coupled conduit and atmospheric dispersal dynamics of the AD 79 Plinian eruption of Vesuvius. *Journal of Volcanology and Geothermal Research*, *120*(1-2), 141–160.
Pyle, D. (1989). The thickness, volume and grainsize of tephra fall deposits. *Bulletin of Volcanology*, *51*(1), 1–15.
Quareni, F., Ventura, G., & Mulargia, F. (2001). Numerical modeling of the transition from fissure-to central-type activity on volcanoes: a case study from Salina Island, Italy. *Physics of the Earth and Planetary Interiors*, *124*(3-4), 213–221.
Santacroce, R., Cioni, R., Marianelli, P., Sbrana, A., Sulpizio, R., Zanchetta, G., et al. (2008). Age and whole rock–glass compositions of proximal pyroclastics from the major explosive eruptions of Somma-Vesuvius: A review as a tool for distal tephrostratigraphy. *Journal of Volcanology and Geothermal Research*, *177*(1), 1–18.
Scaillet, B., Pichavant, M., & Cioni, R. (2008). Upward migration of Vesuvius magma chamber over the past 20,000 years. *Nature*, *455*(7210), 216–219. https://doi.org/10.1038/nature07232
Shea, T., Gurioli, L., & Houghton, B. (2012). Transitions between fall phases and pyroclastic density currents during the AD 79 eruption at Vesuvius: building a transient conduit model from the textural and volatile record. *Bulletin of Volcanology*, *74*(10), 2363–2381.
Shea, T., Gurioli, L., Houghton, B. F., Cioni, R., & Cashman, K. V. (2011). Column collapse and generation of pyroclastic density currents during the AD 79 eruption of Vesuvius: The role of pyroclast density. *Geology*, *39*(7), 695–698.
Shea, T., Houghton, B., Gurioli, L., Cashman, K., Hammer, J., & Hobden, B. (2010). Textural studies of vesicles in volcanic rocks: an integrated methodology. *Journal of Volcanology and Geothermal Research*, *190*(3), 271–289.
Shea, T., Larsen, J., Gurioli, L., Hammer, J., Houghton, B., & Cioni, R. (2009). Leucite crystals: surviving witnesses of magmatic processes preceding the 79AD eruption at Vesuvius, Italy. *Earth and Planetary Science Letters*, *281*(1), 88–98.
Sheridan, M., Barberi, F., Rosi, M., & Santacroce, R. (1981). A model for Plinian eruptions of Vesuvius. *Nature*, *289*(5795), 282.
Sigurdsson, H., Carey, S., Cornell, W., & Pescatore, T. (1985). The Eruption of Vesuvius in A.D. 79. *National Geographic Research*, *1*, 1–55.
Sigurdsson, H., Cornell, W., & Carey, S. (1990). Influence of magma withdrawal on compositional gradients during the AD 79 Vesuvius eruption. *Nature*, *345*(6275), 519.
Spieler, O., Kennedy, B., Kueppers, U., Dingwell, D., Scheu, B., & Taddeucci, J. (2004). The fragmentation threshold of pyroclastic rocks. *Earth and Planetary Science Letters*, *226*(1-2), 139–148.
Sulpizio, R., Cioni, R., Di Vito, M. A., Mele, D., Bonasia, R., & Dellino, P. (2010). The Pomici di Avellino eruption of Somma-Vesuvius (3.9 ka BP). Part I: stratigraphy, compositional variability and eruptive dynamics. *Bulletin of Volcanology*, *72*(5), 539–558.
Valentine, G. A., Krier, D. J., Perry, F. V., & Heiken, G. (2007). Eruptive and geomorphic processes at the Lathrop Wells scoria cone volcano. *Journal of Volcanology and Geothermal Research*, *161*(1-2), 57–80.
Valentine, G. A., & White, J. D. (2012). Revised conceptual model for maar-diatremes: Subsurface processes, energetics, and eruptive products. *Geology*, *40*(12), 1111–1114.
Varekamp, J. C. (1993). Some remarks on volcanic vent evolution during plinian eruptions. *Journal of Volcanology and Geothermal Research*, *54*(3-4), 309–318.
Vinkler, A., Cashman, K., Giordano, G., & Groppelli, G. (2012). Evolution of the mafic Villa Senni caldera-forming eruption at Colli Albani volcano, Italy, indicated by textural analysis of juvenile fragments. *Journal of Volcanology and Geothermal Research*, *235*, 37–54.
White, J. D., & Valentine, G. A. (2016). Magmatic versus phreatomagmatic fragmentation: absence of evidence is not evidence of absence. *Geosphere*, *12*(5), 1478–1488.
Wohletz, K. H. (1986). Explosive magma-water interactions: Thermodynamics, explosion mechanisms, and field studies. *Bulletin of Volcanology*, *48*(5), 245–264.